# Constraints on Uranus's haze structure, formation and transport

Daniel Toledo, Patrick G.J. Irwin, Pascal Rannou, Nicholas Teanby, Amy Simon, Michael Wong, Glenn S. Orton

▶ **To cite this version:**

Daniel Toledo, Patrick G.J. Irwin, Pascal Rannou, Nicholas Teanby, Amy Simon, et al.. Constraints on Uranus's haze structure, formation and transport. Icarus, 2019, 333 (6), pp.1-11. 10.1016/j.icarus.2019.05.018 . hal-02288904

**HAL Id: hal-02288904**

**https://hal.univ-reims.fr/hal-02288904v1**

Submitted on 20 Dec 2023

**HAL** is a multi-disciplinary open access archive for the deposit and dissemination of scientific research documents, whether they are published or not. The documents may come from teaching and research institutions in France or abroad, or from public or private research centers.

L'archive ouverte pluridisciplinaire **HAL**, est destinée au dépôt et à la diffusion de documents scientifiques de niveau recherche, publiés ou non, émanant des établissements d'enseignement et de recherche français ou étrangers, des laboratoires publics ou privés.

Distributed under a Creative Commons Attribution 4.0 International License

Icarus 333 (2019) 1–11

Contents lists available at ScienceDirect

Icarus

journal homepage: www.elsevier.com/locate/icarus

# Constraints on Uranus's haze structure, formation and transport

Daniel Toledo[a,*], Patrick G.J. Irwin[a], Pascal Rannou[b], Nicholas A. Teanby[c], Amy A. Simon[d], Michael H. Wong[e], Glenn S. Orton[f]

[a] Atmospheric, Oceanic and Planetary Physics, University of Oxford, UK
[b] GSMA, UMR 7331-GSMA, Universite de Reims Champagne-Ardenne, 51687 Reims, France
[c] School of Earth Sciences, University of Bristol, Wills Memorial Building, Queens Road, Bristol BS8 1RJ, UK
[d] NASA Goddard Space Flight Center, Solar System Exploration Division (690), Greenbelt, MD 20771, USA
[e] University of California at Berkeley, Astronomy Department, Berkeley, CA 947200-3411, USA
[f] Jet Propulsion Laboratory, California Institute of Technology, 4800 Oak Grove Drive, Pasadena, CA 91109, USA

ARTICLE INFO

*Keywords:*
Uranus
Haze microphysics
Radiative transfer

ABSTRACT

Microphysical simulations have been performed to constrain the formation and structure of haze in Uranus's atmosphere. These simulations were coupled to a radiative-transfer code to fit observations performed by the SINFONI Integral Field Unit Spectrometer on the Very Large Telescope (VLT) and by the Wide Field Camera 3 (WFC3) of the Hubble Space Telescope (HST) in 2014. Our simulations yield an effective radius of $\sim 0.2\,\mu$m for the haze particles in the tropopause and a density of $\sim 2.9$ particles per cm$^3$. Our simulations also provide an estimate for the haze production rate in the stratosphere of between $\sim 3.10^{-16}$ and $3.10^{-15}$ kg m$^{-2}$ s$^{-1}$, about 100 times smaller than that found in Titan's atmosphere (e.g. Rannou et al., 2004). This range of values is very similar to that derived by Pollack et al. (1987) from Voyager-2 observations in 1986, suggesting microphysical timescales greater than the elapsed time between these observations (28 years, or 1/3 of a Uranian year). This result is in agreement with analyses performed with our microphysical model that show timescales for haze particles to grow and settle out to be $> \sim 30$ years at pressure levels $> 0.1$ bar. However, these timescales are too big to explain the observed variations in the haze structure over Uranus's northern hemisphere after 2007 equinox (e.g. de Pater et al., 2015). This indicates that dynamics may be the main factor controlling the spatial and temporal distribution of the haze over the poles. A meridional stratospheric transport of haze particles with winds velocities $> \sim 0.025$ m s$^{-1}$ would result in dynamics timescales shorter than 30 years and thus may explain the observed variations in the haze structure.

## 1. Introduction

Voyager-2 observations revealed the presence of hazes in the atmosphere of Uranus (Pollack et al., 1987; Rages et al., 1991). As in Jupiter and Titan's atmospheres, the haze formation is attributed to photochemical processes that take place in the stratosphere. Methane dissociation by solar UV and energetic particles leads to a network of chemical reactions, producing more complex hydrocarbons (Atreya and Romani, 1985; Moses et al., 2018; Pollack et al., 1987). In the cold stratosphere of Uranus (Tyler et al., 1986), many of these species condense, perhaps continuing to be photolytically processed in the solid state. In addition to condensing ices of acetylene, ethane, and diacetylene that were considered by all prior photochemical models (Orton et al., 2014b; Pollack et al., 1987), Rages et al. (1991) also discussed condensation of $C_6H_2$, while Moses et al. (2005) also discussed condensation of $C_3H_8$, $C_4H_10$, and $C_6H_6$. These species have condensation levels in the 0.1 to 20-mbar region.

A number of radiative-transfer codes have been used to constrain the haze properties in Uranus's atmospheres by fitting observations from ground-based telescopes (or observations from telescopes in orbit around the earth) (e.g. Irwin et al., 2012b; Irwin et al., 2017; Irwin et al., 2016; Karkoschka and Tomasko, 2009; Sromovsky et al., 2011; Sromovsky et al., 2018; Toledo et al., 2018). Although all these analyses required hazes in their respective models to fit the observations, the haze properties (vertical distribution or scattering properties) used or retrieved by the models were very different. For example, Irwin et al. (2016) analyzed VLT spectra in the H-band (1.4–1.8 $\mu$m) using a simple two-cloud model, consisting of a vertically-thin deep cloud near the 2-bar level, together with a vertically-extended haze; meanwhile Sromovsky et al. (2011) used a model consisting of three vertically-thin

* Corresponding author at: University of Oxford, Clarendon Laboratory, Parks Road, Oxford OX1 3PU, UK.
*E-mail address:* daniel.toledocarrasco@physics.ox.ac.uk (D. Toledo).

https://doi.org/10.1016/j.icarus.2019.05.018
Received 19 November 2018; Received in revised form 14 May 2019; Accepted 17 May 2019
Available online 24 May 2019
0019-1035/ © 2019 The Authors. Published by Elsevier Inc. This is an open access article under the CC BY license (http://creativecommons.org/licenses/BY/4.0/).

clouds in the lower troposphere, together with a vertically-extended tropospheric haze from 1 0.1 bar, and a vertically-extended stratospheric haze from 0.1 0.01 bar. Based on the $\chi^2$ results, it was found that both aerosol models provide good fits to the observations despite their different vertical distribution. Similar conclusions were found by Sromovsky et al. (2018), who used several different aerosol models to fit HST-STIS, Keck-NIRC2, and IRTF-SpeX observations. These different radiative-transfer analyses show the limitations of determining precisely the vertical structure of the haze from remote observations alone.

Haze microphysical codes have been used to constrain the haze formation and structure in different atmospheres (e.g. Cabane et al., 1992; Cheng et al., 2017; Pollack et al., 1987; Rannou et al., 2004). By simulating the time evolution of the haze concentration, modelled in terms of number of particles of different sizes at different altitudes, they provide vertical profiles of haze density and size distribution as a function of different input parameters. For instance, Pollack et al. (1987) analyzed Voyager-2 observations with the microphysical model of Toon et al. (1980) and radiative-transfer simulations to constrain the production rate and structure of the haze in Uranus's atmosphere. Although this analysis put strong constraints on the haze structure, a number of recent observations have revealed seasonal changes in Uranus's atmosphere after the 2007 equinox (e.g. de Pater et al., 2015; Sromovsky et al., 2018; Toledo et al., 2018). These observations and analyses pointed to the need of performing new simulations of the formation and growth of haze in Uranus's atmosphere. In this work we analyzed observations acquired in 2014 with a microphysical model to constrain the haze structure in Uranus's atmosphere and also constrain the haze microphysics timescales. In order to better constrain the haze parameters, the haze microphysical simulations were coupled to the NEMESIS radiative-transfer code (Irwin et al., 2008) to model the observations. We describe the data used in this work, the microphysical model, and radiative-transfer codes in section 2. In section 3, we present our model results, compare them to data, and discuss the impact of dynamics on the distribution of the haze in Uranus's atmosphere.

## 2. Observations, haze microphysics and radiative transfer

### 2.1. Observations

We analyzed observations of Uranus in the H-band (1.4–1.8 $\mu$m) performed by the SINFONI Integral Field Unit Spectrometer on the Very Large Telescope (VLT) on 31 October and 11 November 2014 (Irwin et al., 2016). These observations used adaptive optics to achieve a spatial resolution of about 0.1″, returning 64 × 64-pixel spectral cubes, and a spectral resolution $\Delta\lambda$ of 0.0005 $\mu$m. Data reduction was carried out with the ESO VLT SINFONI pipeline and additional photometric corrections as described by Irwin et al. (2016) were also included. The reduced data were then averaged with a triangular-shaped instrument function with Full Width Half Maximum (FWHM) = 0.002 $\mu$m, resulting in a final spectral resolution of R ~775. It was found in previous analyses of Uranus that this spectral resolution provides the best compromise between modelling computational speed, signal-to-noise (SNR) ratio and accurate representation of the methane absorption features (Irwin et al., 2012a).

To better constrain the haze microphysics parameters we also analyzed observations made with the Wide Field Camera 3 (WFC3) of the Hubble Space Telescope (HST) as part of of the Hubble 2020: Outer Planet Atmospheres Legacy program, OPAL. These observations were made in seven spectral channels, detailed in Table 1, on 8 and 9 November 2014 (Wong et al., 2015). The HST/WFC3 photometric errors were computed taking into account: 1) the uncertainty of the photometric calibration of the WFC3 instrument (Dressel, 2012); 2) the uncertainty in the correction for fringing in narrowband filter images at wavelengths longer than ~675 nm (Wong, 2010); and the uncertainty in the solar spectrum (Colina et al., 1996). We added an additional 3.1% uncertainty for quad filters (filters with a 'Q' in their names in Table 1), because the major photometric calibration update for WFC3 in 2016 did not include new flatfields or zeropoints for these filters (Ryan Jr et al., 2016).

**Table 1**
HST/WFC3 filters used in our study.

| Name | λ(nm) | FWHM (nm) | Photometric error (%) |
|---|---|---|---|
| F467M | 467 | 21.5 | 5.1 |
| F547M | 547 | 70.9 | 5.1 |
| FQ619M | 619 | 6.1 | 6.0 |
| F658M | 658 | 2.8 | 5.1 |
| FQ727M | 727 | 6.5 | 6.5 |
| F845M | 845 | 87.6 | 5.1 |
| FQ924N | 924 | 8.9 | 6.5 |

### 2.2. Microphysics

A haze microphysical model developed originally for Titan (Cabane et al., 1992; Rannou et al., 2004) was used in this study to simulate the formation and evolution of haze in Uranus's atmosphere. This one-dimensional Eulerian model solves the aerosol continuity equation subject to eddy diffusion, settling and coagulation, to evaluate the time evolution of the haze number density, $C(r,z)$, described in terms of the particle radius, $r$, and altitude, $z$. Since the model we employ is well documented already (Cabane et al., 1992; Toon et al., 1988; Toon et al., 1980) we shall give only a brief description. The aerosol continuity equation is given by

$$\frac{\partial C(r,z)}{\partial t} = Q(z) + \left[\frac{\partial C(r,z)}{\partial t}\right]_{\text{transport}} + \left[\frac{\partial C(r,z)}{\partial t}\right]_{\text{collection}} \quad (1)$$

The first term of the right side of the equation, $Q(z)$, represents the production of particles (number of particles per unit volume and time) due to photochemical reactions in Uranuss stratosphere. This production is parameterized assuming a Gaussian function whose vertical variation is given by

$$Q(z) = Q(z_0)\exp\left(-\frac{(z-z_0)^2}{2\Delta z^2}\right) \quad (2)$$

where $z$ is the altitude, and $z_0$ and $\Delta z$ are adjustable parameters that characterize the haze production region in Uranus's atmosphere (Pollack et al., 1987). In order to cover the region where the products of $CH_4$ dissociation are expected to condense, the parameter $z_0$ was set to the altitude corresponding to the 0.1-mbar level and a value of $\Delta z$ to 40 km. This choice of parameters defines a production region comprised between the 0.01 and 1-mbar levels. Although our haze production rate parametrization is simplistic (a more complete treatment would need to include separate condensation rates for the various hydrocarbon ices), in section 3.3 we will show that $z_0$ does not have a major impact on the retrievals for $p(z_0) < 118$ mbar. The term $Q(z_0)$ is given by

$$Q(z_0) = \frac{M_0}{(4/3)\pi\rho r_0^3}\frac{1}{\sqrt{2\pi}\Delta z} \quad (3)$$

where $M_0$ is the vertically-integrated production rate (kg m$^{-2}$ s$^{-1}$), $r_0$ is the initial model radius that represents the smallest size (set to 0.0012 $\mu$m) and $\rho$ is the density of the material making up the particles. We tested different initial model radii and we found that this minimum size does not have a major effect on the simulations. The main reason is that the haze particles with such small radii grow in size very quickly due to coagulation. Based on the properties of hydrocarbon ices a value of 0.7 g cm$^{-3}$ was used for $\rho$ (Pollack et al., 1987). The parameter $M_0$ determines the amount of haze particles produced in the high atmosphere and its range of values for Uranus was estimated in our simulations. The second term of the right side of Eq. (1) represents the rate of change of the concentration of particles (for a given size) due to vertical transport. This rate is given by

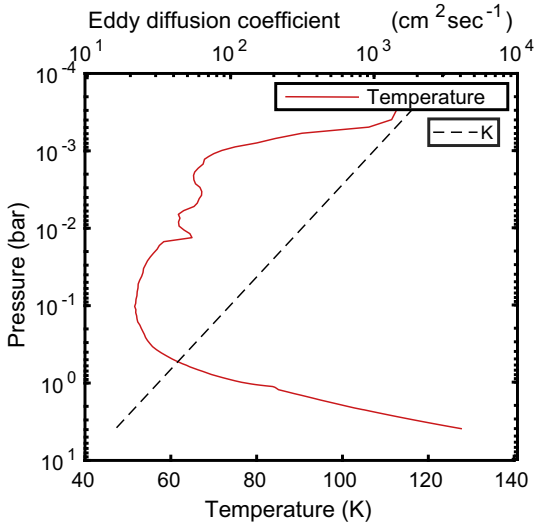


**Fig. 1.** Variation of temperature and eddy diffusion coefficient with height in Uranus's atmosphere.

$$\left[\frac{\partial C(r,z)}{\partial t}\right]_{\text{transport}} = -\frac{\partial}{\partial z}(\phi_{\text{settling}} + \phi_{\text{diffusion}}) \tag{4}$$

where $\phi_{settling}$ and $\phi_{diffusion}$ are the sedimentation and eddy-diffusion fluxes, respectively. The sedimentation flux is calculated from the settling velocities (Cabane et al., 1992), while the eddy-diffusion flux is computed by

$$\phi_{\text{diffusion}} = -K\rho_a \frac{\partial}{\partial z}\left(\frac{C(r,z)}{\rho_a}\right) \tag{5}$$

where $\rho_a$ is the atmospheric density and $K$ is the eddy-diffusion coefficient. In this work we have used the following expression to compute the eddy-diffusion profile in the atmosphere

$$K(p) = K_0\left(\frac{p}{kT}\right)^{-0.5} \tag{6}$$

This expression assumes that the eddy-diffusion coefficient $K(p)$ is proportional to the amplitude of breaking waves ($K(p) = \propto n(p)^{-0.5}$). Therefore, the only free parameter required to compute the eddy-diffusion coefficient at differentaltitudes is $K_0$, whose value is estimated from $K$ at a given reference pressure level. Fig. 1 shows the temperature and eddy-diffusion coefficient profiles used in this work. The temperature profile is based on the 'F1' profile computed by Sromovsky et al. (2011), and $K$ profile was computed using Eq. (6); $K_0$ was derived from the value of $K$ at the $4 - 2 \times 10^{-5}$-bar level given in Fouchet et al. (2003) ($\sim 1 \times 10^4\,\text{cm}^2 s^{-1}$). Compared to the other giant planets, Uranus's atmosphere seems to be particularly sluggish (K is about 10 times bigger for Neptune's atmosphere). The last term of the right side of Eq. (1) represents the change of concentration of the particles with a given size due to collection (coagulation and coalescence). This term can be expressed as

$$\left[\frac{\partial C(r,z)}{\partial t}\right]_{\text{collection}} = \left[\frac{\partial C(r,z)}{\partial t}\right]_{\text{source}} - \left[\frac{\partial C(r,z)}{\partial t}\right]_{\text{sink}} \tag{7}$$

The two terms on the right side of the equation represent the creation and loss rates of particles of a given size $r$; the creation of particles of size $r$ by collection of particles of smaller sizes; the loss rate of particles of size $r$ by collection with particles of any size. For the haze microphysics, the gravitational collision-coalescence processes can be neglected and the collection kernel $K_c$, required to compute both rates (see Cabane et al., 1992), accounts only for coagulation. This coefficient is computed for spherical particles using classical assumptions (Fuchs, 1964). For modelling the coagulation rate in a given radius bin, we need to specify the sticking coefficient (Pollack et al., 1987), whose value for two particles of radius $r_1$ and $r_2$ is given by

$$s = \exp\left(\frac{-q^2 r_1 r_2}{kT(r_1 + r_2)}\right) \tag{8}$$

where $T$ is the temperature, $k$ is the Boltzmann's constant and $q$ is the haze charge-per-unit-radius parameter (expressed in electrons per micrometre of radius). The sticking coefficient represents the probability that two haze particles will stick together. Since no reliable information concerning the charge of Uranus's haze particles is available, this parameter, $q$, was also derived in our simulations. For a set of values of $M_0$, $q$ and $K_0$ the code computes the vertical distribution of the number density and size distribution of the haze particles by simulating the processes of eddy diffusion, coagulation and settling. How fast these different processes interact depend on $M_0$, $q$ and$K_0$, and their respective timescales will be discussed in section 3.3.

### 2.3. Radiative transfer

The NEMESIS correlated-k radiative-transfer and retrieval code (Irwin et al., 2008) was used to simulate the scattering and absorption of gases and aerosols in Uranus's atmosphere. The same atmospheric model as described in Irwin et al. (2018) and Irwin et al. (2017) was used to model the spectra. The temperature profile was based on the 'F1' profile computed by Sromovsky et al. (2011), which assumes an He:$H_2$ ratio of 0.131, a mole fraction of neon of 0.004% and a tropospheric $CH_4$ mole fraction of 4% atnon-polar latitudes. The methane absorption in the H-band was computed using the 'WKMC-80K' line database (Campargue et al., 2012), while for HST observations, for which WKMC-80K is not appropriate, we used the methane absorption coefficients of Karkoschka and Tomasko (2010). The methane line data and band data were converted to k-distribution look-up tables. The VLT observations were smoothed assuming a triangular-shaped instrument function with full width half maximum = 0.002 $\mu$m, while for the HST observations we used filter-averaged k-tables. Collision-induced absorption by $H_2$–$H_2$ and $H_2$–He was computed using the coefficients of Borysow et al. (2000), Borysow et al. (1989) and Zheng and Borysow (1995), and an equilibrium ortho/para-$H_2$ fraction was assumed at all altitudes and locations. Absorption by $H_2$–$CH_4$ and $CH_4$–$CH_4$ collision-induced was also computed (Borysow and Frommhold, 1987).

## 3. Analysis procedure and results

### 3.1. Analysis procedure

To determine the haze parameters described in section 2.2, we coupled the microphysics haze simulations with the NEMESIS radiative-transfer code. For a given latitude, we fitted VLT and HST observations with NEMESIS using a cloud model comprising a thick tropospheric cloud and a haze layer whose size distribution and density profiles were computed with the microphysical model for a set of values of$M_0$, $q$ and $K_0$. At each altitude, the haze size distribution computed by the microphysical model is fitted to a log-normal size distribution as illustrated in Fig. 2. The haze and cloud-scattering parameters required for the radiative-transfer simulations (single-scattering albedo, phase function, and extinction cross section) were computed at all wavelengths using Mie theory, where we fitted (as a part of the NEMESIS inversion) the refractive index spectrum of the haze particles. Similar to previous analyses (see Irwin et al., 2018; Toledo et al., 2018), the effective radius of the tropospheric cloud particles was fixed to 1 $\mu$m and their vertical distribution was characterised by the total opacity (free parameter), the fractional scale height (defined as the ratio of the scale height of the aerosol density to the scale height of the bulk atmosphere, and whose value is fixed to 0.01), and the cloud altitude (fixed to the 2-bar pressure level). However, as will be shown in section 3.2, the choice

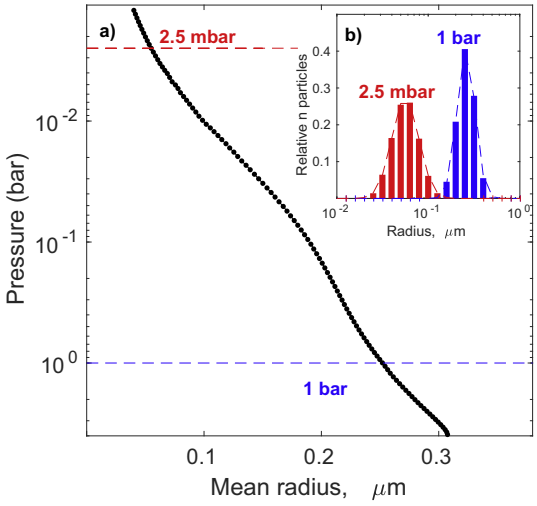


**Fig. 2.** (a) Haze mean-radius profile computed by fitting at each altitude the size distribution given by the microphysical model to a log-normal size distribution. (b) The blue and red bars represent the relative number of particles in each radius bin computed with microphysical model and the dashed lines correspond to the distribution obtained by fitting the profiles. (For interpretation of the references to colour in this figure legend, the reader is referred to the web version of this article.)

of the cloud altitude and structure does not have a major impact on the haze retrievals. For each instrument wavelength range, the spectrum of the imaginary refractive index was retrieved at two wavelengths (the values at all other wavelengths were computed by a linear interpolation), and the real part of the refractive index at 1.4 $\mu$m was set to a reference value of 1.4 (see Irwin et al., 2018; Irwin et al., 2017); the real part of the refractive index at all other wavelengths was calculated using the Kramers-Kronig relation (see Sheik-Bahae, 2005).

The free parameters in our analysis are, therefore, the haze parameters $M_0$, $q$ and $K_0$, the tropospheric cloud total opacity, and the imaginary refractive index of both aerosol layers. Fig. 3a–b shows, as an example, a number of haze size distribution and density profiles computed for different values of $M_0$. These simulations show that an increase in the stratosphere haze production results in a greater number density and mean particle radius at all the atmospheric levels. This points out that even if we cannot detect the haze particles at high altitudes due to their small size, the haze production rate can be derived from the light reflected by the haze at lower levels where the particles are bigger in radius. This can also be observed in Fig. 3c–d that shows the cumulative scattering optical depth ($\tau$) at 1.4 $\mu$m computed for the size distribution and density profiles illustrated in Fig. 3a–b, and simulations of VLT data at 5°S (Fig. 3d). The red line in Fig. 3d shows a fit using the haze profiles computed for $M_0 = 9.10^{-16}$ kg m$^{-2}$ s$^{-1}$ (red dashed lines in Fig. 3a–b), while the black, red and purple lines are simulations using the same free parameters as for the red case, but for different haze production rates. The grey, shaded line represents the VLT observations with errors. Our model indicates that an increase in the haze production results in a greater scattering optical depth (Fig. 3c) and hence, a higher reflectance (Fig. 3d). Note that: a) we can derive $M_0$ due to the variations in the haze scattering optical depth with the haze production; b) the vertical profiles of haze number density and mean radius can be constrained using the microphysical model; c) VLT wavelengths with strong methane absorption are more sensitive to variations in the haze production rate since most of the light is reflected at the upper levels of the atmosphere. Therefore, these results show that by analysing our observations with both haze-production and radiative-transfer models we can constrain the microphysical parameters and hence, the haze structure (vertical profiles of density and size) in Uranus's atmosphere.

### 3.2. Results

In order to speed up the simulations, the retrieval procedure makes use of a pre-computed set of look-up tables of the haze density and size distribution for a number of combinations of $M_0$, $q$ and $K_0$. For each haze density and size profile, we fitted the VLT and HST observations at latitudes between 5°S and 20°N with the NEMESIS code. Therefore, for each $M_0 - q - K_0$ combination, we retrieved the imaginary refractive index of the tropospheric cloud and the haze, and the tropospheric cloud opacity as described in the previous section. Fig. 4 shows an analysis performed at ~5°S. This latitude was selected to compare our retrievals with those given in Pollack et al. (1987). The upper panel shows examples of VLT and HST images of Uranus and indicates the pixels (red dots) selected for the analysis. The lower panel shows contours of $\chi_{red}^2$ in the $M_0 - q$ parameter space carried out at the selected pixels and using the $K$ profile illustrated in Fig. 1. The lower panel of Fig. 4 also shows the $\sigma$, $2\sigma$ and $3\sigma$ significance levels of $\chi_{red}^2$ (white lines), and the range of $M_0$ determined by Pollack et al. (1987) from Voyager-2 observations at similar latitudes (purple line). A similar contour plot was made for the coefficient $K_0$. However, we found that for the $K_0$ range of values expected for Uranus's atmosphere, this

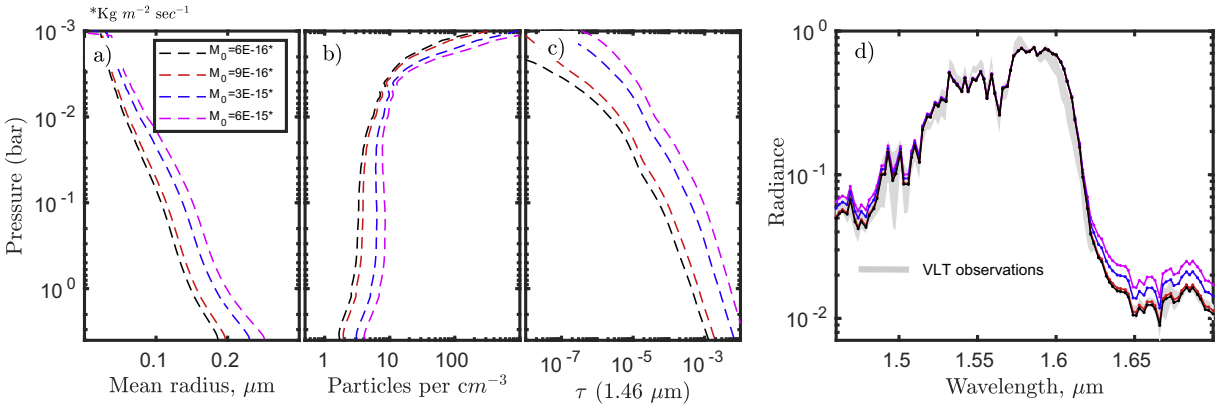


**Fig. 3.** (a)–(b) Vertical profiles of haze mean-radius and number density computed with the microphysical model using different values of the production rate. (c) Scattering optical depth at 1.46 $\mu$m computed for the haze size and number density profiles shown in (a)–(b), and a haze refractive index of n = 1.4 + 0.0001i. (d) Comparison between NEMESIS simulations and VLT observations at 5°S. The thick grey solid line represents VLT observations at 5°S. The VLT spectrum was fitted using the cloud model discussed in section 3 for a haze production rate and electric charge of $\mathbf{9 \times 10^{-16}}$ kg m$^{-2}$ s$^{-1}$ and 10 electrons per $\mu$m radius, respectively (red dotted line). The black, blue and purple dotted lines are VLT simulations when only the haze profiles are changed. (For interpretation of the references to colour in this figure legend, the reader is referred to the web version of this article.)

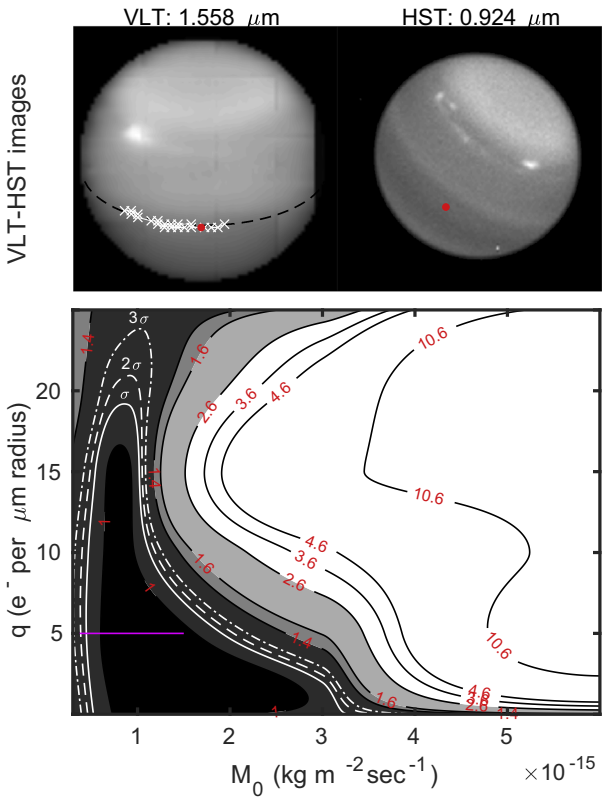


**Fig. 4.** (Upper) Very Large Telescope (VLT) and Hubble Space Telescope (HST) images at 1.558 and 0.924 $\mu$m made on 31 October and 9 November 2014, respectively. (Lower) Contours of $\chi^2_{red}$ in the $M_0 - q$ parameter space for the fits performed at 5°S (red dots of VLT and HST images). The red purple line represents the range of $M_0$ values estimated by Pollack et al. (1987) from Voyager-2 observations. The white crosses in the upper panel indicate the pixels analyzed in Fig. 6. (For interpretation of the references to colour in this figure legend, the reader is referred to the web version of this article.)

parameter does not have a significant effect on the haze profiles. In the next subsection, the effect of a possible increase in $K$ in the troposphere on the retrievals will be discussed. Since variations in the temperature may change the sticking coefficient or the settling velocities, we also performed these simulations using the global average temperature structure derived from Spitzer IRS observations (Orton et al., 2014a). We found that both temperature profiles provide similar results.

The contour lines of $\chi_{red}^2$ shown in Fig. 4 indicate that the best solutions are found for $M_0$ values of between $3.10^{-16}$ and $3.10^{-15}$ kg m$^{-2}$ s$^{-1}$, and $q$ smaller than ~20 electrons per $\mu$m radius (assuming a significance level of $2\sigma$ for $\chi_{red}^2$). We also observe that this range of optimal $M_0$ values is very similar to that found by Pollack et al. (1987) from Voyager-2 observations at similar latitudes. The average and 1-standard deviation of the haze profiles (size distribution and density) derived for these haze parameters range values are given in Fig. 5. In order to facilitate the use of these profiles for future work, we have fitted each profile with two different functions whose parameters are indicated in Fig. 5. We tested our derived haze profiles at different pixels localized approximately at the same latitude. These pixels are indicated with white crosses in the VLT image shown in the upper panel of Fig. 4. The values of $\chi_{red}^2$ for those pixels are illustrated in the upper panel of Fig. 6. These $\chi_{red}^2$ values represent the differences between the observations and the simulations when using the retrieved aerosol properties at our reference point (see Fig. 4) at all other pixels along the latitude line. Although $\chi_{red}^2$ is larger for the pixels that are further away from the pixel of the analysis of Fig. 4 (red dot), these results show that our aerosol retrievals fit the observations at these other locations reasonably well. This indicates a haze production rate practically constant along the same latitudinal circle.

The results of Fig. 4 indicate that, although the solar illumination at the top of the atmosphere at these latitudes has changed significantly between the Voyager-2 and VLT observations (this variation is shown in Fig. 7), the haze structure has not varied significantly. However, since the haze is a photochemical product, it would be expected that its production rate should vary with the solar illumination at the top of the atmosphere as illustrated in Fig. 7. In addition, these changes in the production rate would result in changes in the albedo of the planet at some specific wavelengths (for instance at 1.7 $\mu$m) as illustrated in Fig. 3. The lower panel of Fig. 6 shows the variation of the intensity with the haze production rate at four different wavelengths. We observe that, while the observations at 1.56 $\mu$m are not sensitive to changes in the production rate, the intensity ratios at 1.46, 1.64 and 1.7 $\mu$m increase with the production of haze. This is because at strong methane-absorbing wavelengths (e.g. at 1.46, 1.64 and 1.7 $\mu$m) only the high troposphere or stratosphere is sampled and hence, these observations are sensitive only to light reflected from upper-level hazes. However, at weak methane-absorbing wavelengths (e.g. at 1.56 $\mu$m) most of the light is reflected by the main cloud deck as a result of its larger opacity. In other words, the haze parameters are retrieved at wavelengths for which the tropospheric cloud deck properties do not have a significant impact on the observations. Therefore, any spatial or temporal variation in the production rate should result in variations in the albedo of the planet at these strong methane-absorbing wavelengths. The analysis illustrated in Fig. 4 shows that the haze vertical profiles (density and size distribution) in 2014 do not reveal a noticeable variation in the haze production rate with respect to Voyager-2 observations. This may suggest that the haze microphysics timescales are greater than the time lag between the Voyager-2 and VLT observations (since the solar illumination at the top of the atmosphere at these latitudes has changed). Another possibility to explain the results given in Fig. 4 is that the main factor controlling the haze distribution is dynamics. Indeed, if the timescales for dynamics are shorter than those for microphysics, then any variations in the haze structure due to variations in the production rate will be much smaller than those due to the transport of particles by dynamics, which in turn could maintain a homogenous distribution of the haze. In the next subsection the timescales of the different processes involved in Eq. (1) and dynamics are studied.

### 3.3. Timescale analysis

We performed a haze microphysics timescale analysis to study how variations in the haze production might affect the haze vertical structure. Fig. 8 shows the timescales for haze to grow and fall to different altitudes in the atmosphere for a given production rate of $3.10^{-15}$ kg m$^{-2}$ s$^{-1}$ and different values of $z_0$ (parameter to define the haze production region in Eq. (2)). The eddy profile illustrated in Fig. 1 was used in these simulations. The model was started at time $t = 0$ with no haze in the atmosphere, and the blue curve represents the steady profile, obtained for $t = 160$ years. The rest of the curves represent the haze profiles obtained after 10, 30, 60, 90 and 120 years (in all the cases starting with no haze at $t = 0$). For example, for $z_0 = z(p = 0.12$ mbar) variations in the haze production rate result in haze concentration variations near the 0.01-bar level 10 years after such a change in the production rate, or at altitudes near the tropopause up to 30 years later. Although the timescales are shorter at higher levels in the atmosphere, note that the contribution of these layers to the total haze opacity is very small compared to that of layers at pressure levels > 0.01 bar. This can be observed in Fig. 9 that shows the variation with pressure of the scattering optical depth at 1.46 $\mu$m (upper panel) and the haze microphysics timescale (lower panel) for a haze production rate of $M_0 = 3.10^{-15}$ kg m$^{-2}$ s$^{-1}$ and the different $z_0$ values used in Fig. 8. For $z_0 = z(p = 0.12$ mbar), $z(p = 1.18$ mbar) and $z(p = 11.8$ mbar) the cumulative optical depth is very similar for $p > 0.05$ bar. Although variations in the optical depth are found at higher levels, as a result of the

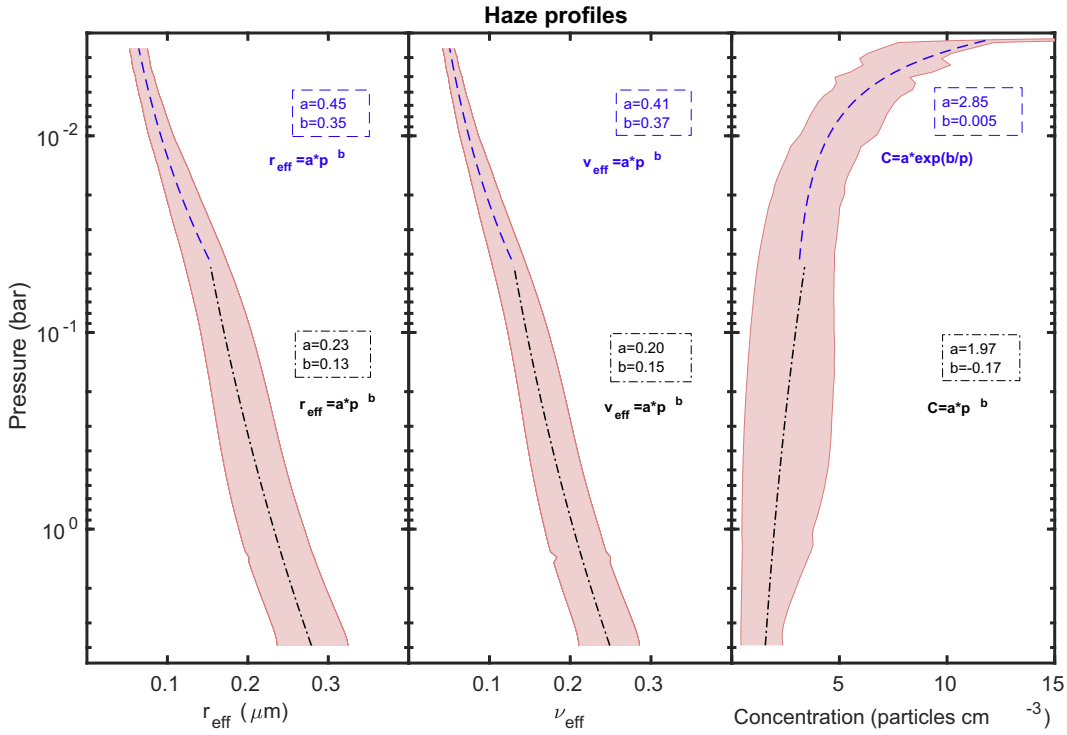


**Fig. 5.** Vertical profiles of the average and 1-standard deviation of the haze size distribution and density computed using the solutions at 5°S given in Fig. 4. The profiles were fitted to empirical functions (illustrated in each panel) at two different pressure levels to facilitate the use of the profiles.

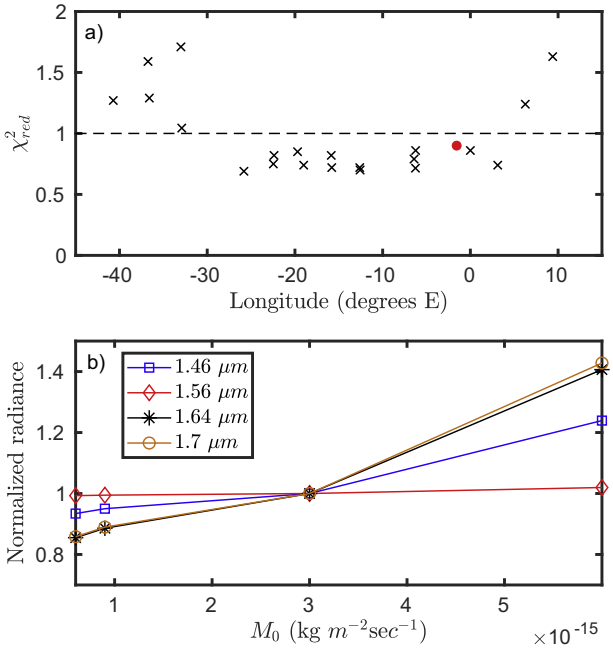


**Fig. 6.** (Upper) Values of $\chi_{red}^2$ obtained when the aerosol properties derived from the analysis illustrated in the lower panel of Fig. 4 are used at different locations. The pixels for this analysis are indicated by white crosses in the upper panel of Fig. 4. (Lower) Radiances at 1.46, 1.56, 1.64 and 1.7 $\mu$m versus haze production rate. The radiances at each wavelengths are normalized to the radiance given for a haze production rate of $3.10^{-15}$ kg m$^{-2}$ s$^{-1}$.

variation in $z_0$, note that the total opacity at those levels is negligible (smaller than $10^{-4}$). The intersections between the black solid line of Fig. 9a and the rest of curves, indicated as *L1* and *L2*, show the pressure levels at which the cumulative optical depth is $5.10^{-4}$ (for smaller values of this optical depth our observations are not sensitive to the haze). Therefore, these results show that with the exception of $z_0 = z$ ($p$ = 118 mbar), possible variations in $z_0$ are not expected to change notably our estimations. Note that the simulations for $z_0 = z$ ($p$ = 118 mbar) represent an extreme case for the production of haze since the products of $CH_4$ dissociation are expected to condense at much higher altitudes. Similar conclusions are found for the haze timescales showed in Fig. 9b, where we observe that for $p > p(L1)$ the timescales for $z_0 = z(p = 0.12$ mbar), $z(p = 1.18$ mbar) and $z$ ($p$ = 11.8 mbar) are very similar.

These results show that the timescales for aerosols to grow and fall are > 30 years at pressure levels > 0.1 bar in Uranus's atmosphere. That is to say, even if the haze production has changed since Voyager-2 observations, these changes in the production rate will not be observed in the haze structure several years later due to the small haze optical depth at the pressure levels where the haze initially condenses. This can be observed in Fig. 10a that shows the pressure levels at which the haze optical depth $\tau_s$ are 0.001 and 0.005 for different haze production rates. These pressure levels clearly show that all wavelengths probe levels much deeper than $p(z_0)$ (the haze production region). We tested this also by increasing linearly the production rate with time for a period of 30 years. We started with the steady haze profiles given for a production rate of $3.10^{-15}$ kg m$^{-2}$ s$^{-1}$, and then we increased the production rate linearly with the time as follows:

$$M_0(t) = M_0(t=0) + \frac{M_0(t = 30\,years) - M_0(t=0)}{30 \times 365 \times 24 \times 3600} \times t \qquad (9)$$

where $M_0(t = 0) = 3.10^{-15}$ kg m$^{-2}$ s$^{-1}$ and $M_0(t = 30\ years)$ is the production rate after 30 years. We run the model for a period of 30 years (simulating the elapsed time between Voyager and VLT observations) for different final values of $M_0(t = 30\ years)$:

$$\Delta M_0 = M_0(t = 30\,years) - M_0(t=0) = 0.2 M_0(t=0)$$

$$\Delta M_0 = M_0(t = 30\,years) - M_0(t=0) = 0.4 M_0(t=0)$$

$$\Delta M_0 = M_0(t = 30\,years) - M_0(t=0) = 0.6 M_0(t=0)$$

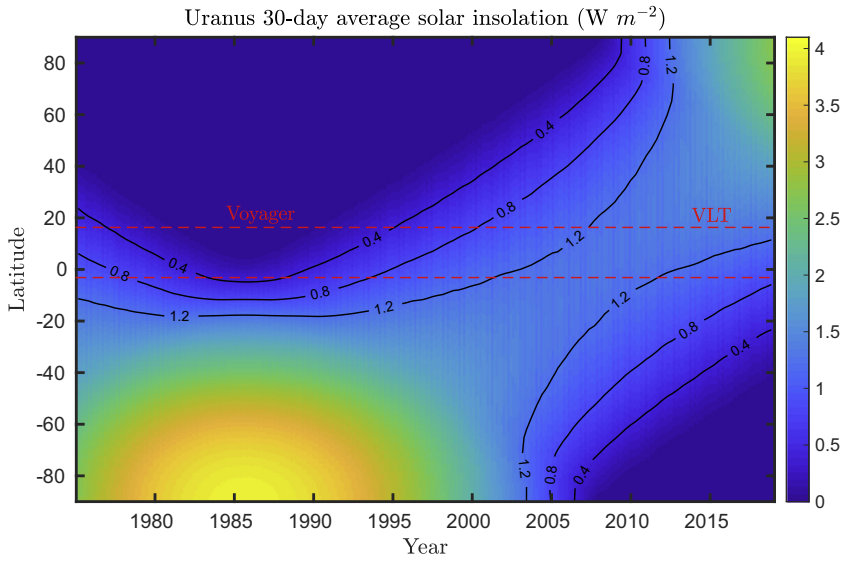


**Fig. 7.** Variation of the 30-day average solar insolation at the top of the atmosphere of Uranus with time.

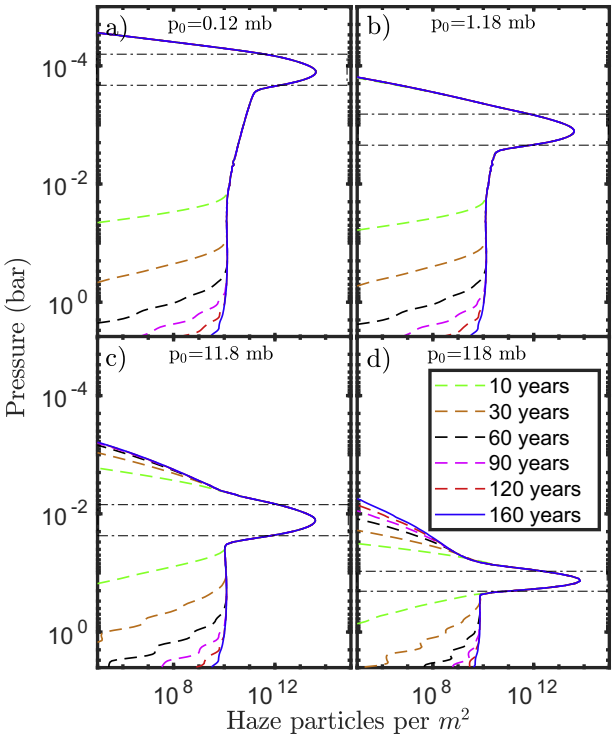


**Fig. 8.** Haze profile computed with our haze microphysical model for different time scales using a haze production rate of $3.10^{-15}$ kg m$^{-2}$ s$^{-1}$ and different altitude levels $z_0$ to characterize the haze production region (see Eq. (2)): $z_0 = z$ ($p$ = 0.12 mbar), $z_0 = z(p$ = 1.18 mbar), $z_0 = z(p$ = 11.8 mbar) and $z_0 = z$ ($p$ = 118 mbar). The haze density is equal to zero for $t$ = **0** and the blue line is the steady profile, obtained for $t$ = **160** years. The rest of curves represent the profiles obtained for different time scales. (For interpretation of the references to colour in this figure legend, the reader is referred to the web version of this article.)

$$\Delta M_0 = M_0(t = 30\,years) - M_0(t = 0) = 1.2 M_0(t = 0)$$

Subsequently, we computed from these haze profiles (number density and size distribution) the scattering optical depth for a constant refractive index of n = 1.4 + 0.0001i. These results are illustrated in Fig. 10b. We observe that changes in the production rate during this time period results in only small variations in the scattering optical

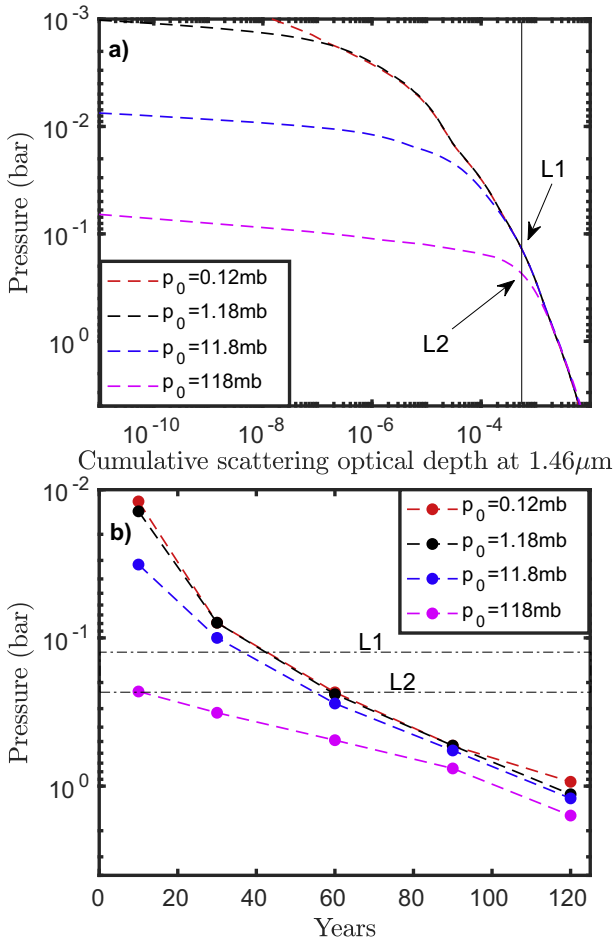


**Fig. 9.** Variation of scattering optical depth at 1.46 $\mu$m (upper panel) and haze microphysics timescale (lower panel) with pressure for a haze production rate $M_0 = 3.10^{-15}$ kg m$^{-2}$ s$^{-1}$, and the different values of $z_0$ showed in Fig. 8. The optical depth was computed for a haze refractive index of n = 1.4 + 0.0001i.

depth. This is due to the large haze microphysics timescales. For instance, at the 1-bar level variations in $M_0$ of 20, 40, 60 and 120% results in variations of the optical depth of $\sim 2.10^{-4}$, $4.10^{-4}$, $5.10^{-4}$, $1.10^{-3}$.

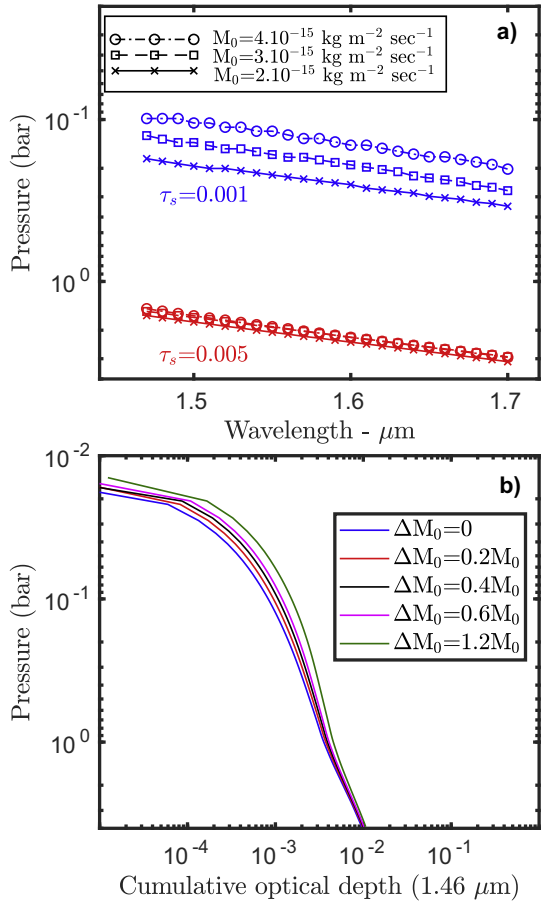


**Fig. 10.** (Upper) Pressure level at which the haze cumulative optical depth $\tau_s$ is 0.001 (blue lines) and 0.005 (red lines) for different haze production rates: $\boldsymbol{M_0}$ = 2.10$^{-15}$, 3.10$^{-15}$ and 4.10$^{-15}$ kg m$^{-2}$ s$^{-1}$. (Lower) Scattering optical depth at 1.46 $\mu$m computed for different $\boldsymbol{\Delta M_0}$ and for a constant refractive index of n = 1.4 + 0.0001i. (For interpretation of the references to colour in this figure legend, the reader is referred to the web version of this article.)

If we take into the account the fact that our observations are sensitive only to haze optical depths bigger than 5.10$^{-4}$ (see levels L1 and L2 of Fig. 9), then we conclude that to observe significant change in the haze structure during these 30 years it is necessary to vary $M_0$ by at least 100%.

In order to further study the different processes that control the evolution of the haze structure, the time rates of the different processes involved in Eq. (1) have been calculated. The timescale of sedimentation, $t_{fall}$, represents the time required for haze particles to fall a distance $H$ (in this work we have used a value of 30 km for $H$ that is the pressure scale height). Therefore, the sedimentation timescale is given by

$$t_{fall} = \frac{H}{v_{fall}} \tag{10}$$

where $v_{fall}$ is the fall velocity whose value depends on the size and density of the particles, the temperature and the number density of the atmosphere. The timescale for eddy diffusion, $t_{diff}$, represents the time required for haze particles to be mixed over a distance H and it is given by

$$t_{diff} = \frac{H^2}{K} \tag{11}$$

where $K$ is given by Eq. (6). Comparing both timescales we can investigate how effectively eddy diffusion can suspend haze particles of a given size $r$ at different altitudes. The other two processes involved in Eq. (1) are the coagulation and production rates. The coagulation timescale, $t_{coag}$, is defined as the time required to reduce the total number of haze particles $n$ by 50% (Toon et al., 1992). Then

$$t_{coag} = \frac{1}{2nK_c} \tag{12}$$

where $K_c$ is the collection kernel. As pointed in Toon et al. (1992), the main problem of using Eq. (12) is that the haze number density $n$ is not easy to constrain from observations. To address this problem, Toon et al. (1992) made use of the mass production time, $t_{mass}$, which is defined for a given size $r$ and mass production $M_0$ as

$$t_{mass} = \frac{4\pi r^3 nH\rho}{3M_0} \tag{13}$$

If we start the model at time $t = 0$ with no haze in the atmosphere, then at each time iteration $\Delta t$ the haze concentration $n_t$ increases and hence,

$$t_{coag}(t=0) > t_{coag}(t=\Delta t) > t_{coag}(t=2{\cdot}\Delta t) > \ldots > t_{coag}(t=i{\cdot}\Delta t)$$

$$t_{mass}(t=0) < t_{mass}(t=\Delta t) < t_{mass}(t=2{\cdot}\Delta t) < \hat{a}\text{€}\text{¦} < t_{mass}(t=i{\cdot}\Delta t)$$

The steady state is achieved at the moment for which both time scales are similar and the haze concentration n is practically constant with time. This time constant, defined as $t_{eqm}$, represents time need to achieve a balance between the production of particles of a given size and the loss due to coagulation. Note that if $t_{coag}$ and $t_{mass}$ are equated, then the number density of haze particles can be derived. In order to compare these different processes, Fig. 11 shows the timescales $t_{fall}$, $t_{diff}$ and $t_{eqm}$ as a function of altitude and for different radii. The time constants were computed for a haze production rate of 3.10$^{-15}$ kg m$^{-2}$ s$^{-1}$ and an electric charge of q = 0. Fig. 12 shows the same as Fig. 11 but for an electric charge of q = 10 electrons per $\mu$m radius. In both figures $t_{diff}$ was computed for two different K profiles; the profile illustrated in Fig. 1 and the same profile but multiplied by a factor of 5 (the timescale derived from this profile is indicated as $t_{diff}^*$). The left-hand panels of both figures indicate that haze particles with radii $r$ = 0.0015 $\mu$m are limited in number by coagulation after 7 days of mass production. For this size the particles remain at the same altitude ($t_{fall}$ and $t_{diff}$ are much larger than $t_{eqm}$) and undergo changes due only to coagulation. As the haze particles grow in size by coagulation, particle removal due to sedimentation takes place, limiting the number of particles of a given size. For instance, the middle panels show that at pressure levels above 1.10$^{-3}$ bar, the times for particles with radii of 0.1 $\mu$m to fall a distance H is much smaller than $t_{eqm}$. We also observe that the timescales $t_{fall}$ and $t_{eqm}$ are very similar at the 0.009-bar level for Fig. 11, and at the 0.016-bar level for Fig. 12. These levels establish, for each case, the altitudes for which particles with radii of 0.1 $\mu$m are transported by sedimentation a distance H in about the time it takes for the mass production to make them. For this particle size the eddy diffusion does not have a major influence over the particles since $t_{diff}$ and $t_{diff}^*$ are much larger than $t_{fall}$ and $t_{eqm}$. For particles with radii of about 0.3 $\mu$m or larger, the sedimentation timescale is much smaller than $t_{eqm}$ and $t_{diff}$ (see right-hand panels of Fig. 11 and Fig. 12). This indicates that these particles are very likely to be found at pressures > 1 bar.

In none of the cases analyzed was the eddy diffusion found to have a major effect on the haze structure (even when the profile illustrated in Fig. 1 is multiplied by a factor of 5). This explains the results of Fig. 4 where we found that the eddy diffusion has a little effect on the retrievals. We also used the stratospheric eddy-diffusion profile given in Orton et al. (2014b) and similar results were found. Furthermore, a possible increase in the eddy-diffusion near the tropopause (instead of the decrease illustrated in Fig. 1) would not change our results as long as K values are smaller than ~10,000 cm$^2$ s$^{-1}$. Fig. 13 shows the fall velocity as a function of altitude for different particle sizes. These fall velocities can be regarded as the vertical wind velocities required to suspend haze particles of a given size at different altitudes. For

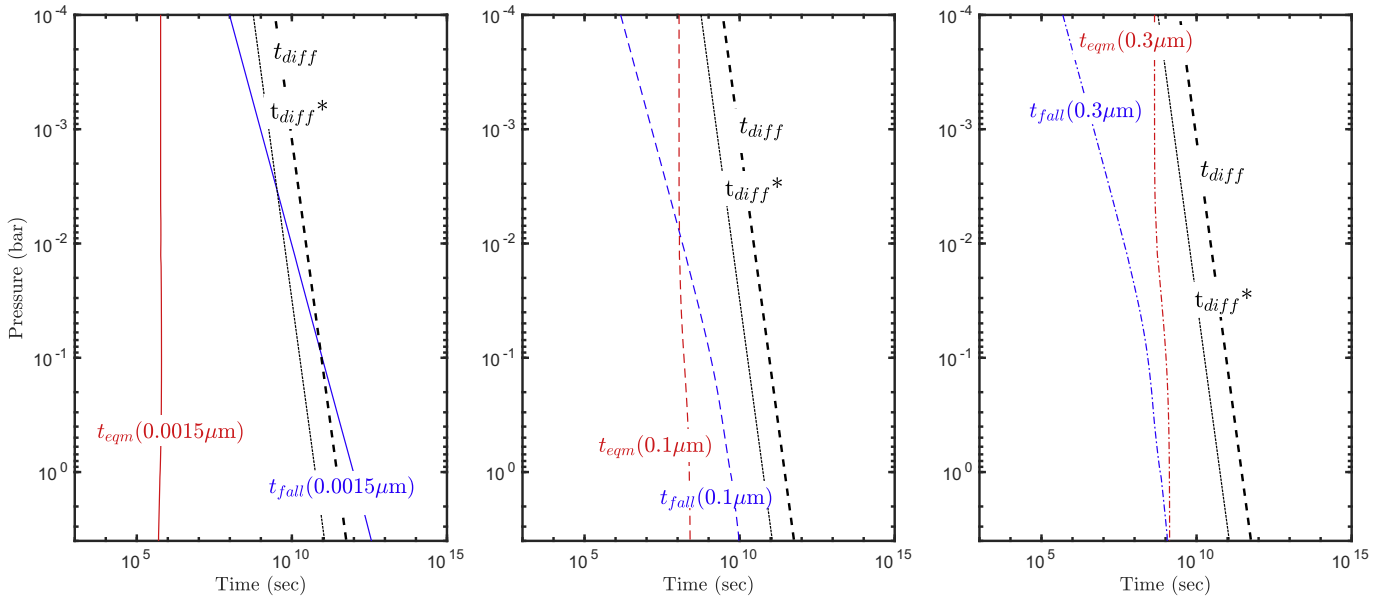


**Fig. 11.** Comparison of the timescales of the different processes involved in Eq. (1) as a function of altitude and for three different particle sizes. The timescales were computed for a haze production rate of $3.10^{-15}$ kg m$^{-2}$ s$^{-1}$ and an electric charge of q = 0. The eddy-diffusion timescale is computed for two K profiles: the profile illustrated in Fig. 1 ($t_{diff}$) and the same profile but multiplied by a factor of 5 ($t_{diff}$*).

example, the results illustrated in Fig. 11 and Fig. 12 have shown that particles with radii of 0.3 $\mu$m or larger are more likely to be found at pressure levels larger than 1 bar. However, Fig. 13 shows that a vertical wind of $\sim 1.10^{-4}$ m $s^{-1}$ or $\sim 8.10^{-4}$ m s$^{-1}$ would be able to suspend these particles at pressure levels above such level. Though these results indicate that the haze particles may easily respond to vertical dynamical motions in upwelling regions (due to the small magnitude of these velocities), annual average estimations show vertical winds in Uranus atmosphere much smaller than those given in Fig. 13 (Conrath et al., 1990). These results point out the need to estimate the vertical winds during the year to fully study whether this vertical haze transport is possible for some time periods.

Post-2007 equinox observations have revealed a number of seasonal changes in the Uranus haze structure over the north pole (de Pater et al., 2015; Sromovsky et al., 2018). Although it can be argued that these variations could be the result of an increase in the photochemical product with the solar cycle, our calculations indicate that these changes occur too quickly to be explained by microphysical processes, and hence they must be due to other factors such as dynamics. Previous works have discussed a possible stratospheric meridional circulation, similar to a Hadley cell, with winds that may transport haze particles from upwelling regions to the North pole. In Fig. 13 we have seen that the haze particles may respond easily to these vertical dynamical motions as a result of the small magnitude of the fall velocities (for the pressure levels studied in this work). These haze particles (lifted by the vertical winds) may be transported by the stratospheric circulation to downwelling regions (North pole). This mechanism is similar to that observed in Titan where the haze is redistributed by the planetary-scale circulation; the haze particles are lifted in the summer hemisphere by ascending stratospheric winds, and then they are transported to the

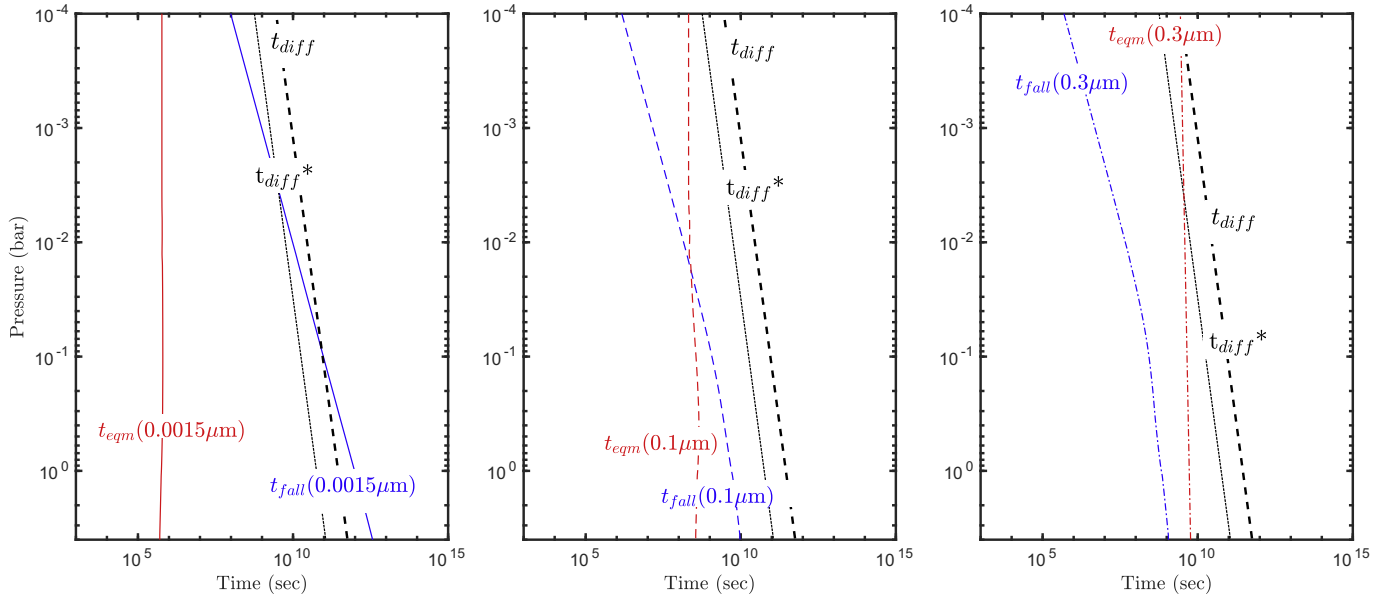


**Fig. 12.** Same as Fig. 11 but for a haze production rate of $3.10^{-15}$ kg m$^{-2}$ s$^{-1}$ and an electric charge of q = 10 electrons per $\mu$m radius.

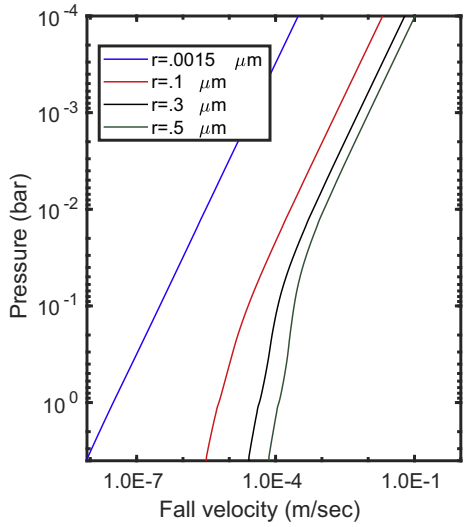


**Fig. 13.** Variation of fall velocity with altitude for haze particles with radii of 0.0015, 0.1, 0.3 and 0.5 $\mu$m.

winter hemisphere where they sink (Rannou et al., 2004). If these seasonal changes in the Uranus haze structure over the north pole are due to this possible meridional circulation, then the timescales for stratospheric meridional transport should be smaller than those given for microphysics (or in terms of velocities that the stratospheric meridional winds are faster than the haze settling velocities). The timescale for a haze particle to be transported a distance equal to the radius of Uranus ($R$) can be estimated using the following expression

$$t = \frac{R}{V} \tag{14}$$

where $V$ is the meridional wind. From Eq. (4) and the timescales shown in Fig. 8, we can compute for each altitude the equivalent wind velocity ($V^*$) that represents the wind velocity for which the timescale for haze meridional transport equals the microphysics timescale. If the meridional wind velocity is larger than the equivalent wind velocity, then the haze spatial distribution and its temporal evolution are mainly dominated by dynamics. Fig. 14 shows the haze microphysics timescales and the equivalent wind velocities as a function of the pressure,

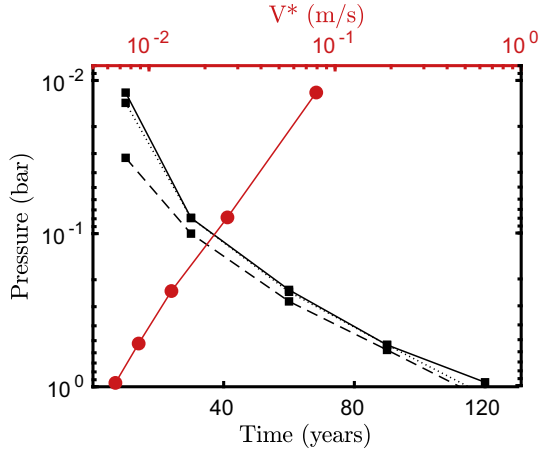


**Fig. 14.** Variation of haze microphysics timescale with pressure for a haze production rate of $3.10^{-15}$ kg m$^{-2}$ s$^{-1}$ and $z_0 = z(p = 0.12\,mbar)$ (black solid line), $z_0 = z(p = 1.18\,mbar)$ (black dotted line) and $z_0 = z(p = 11.8\,mbar)$ (black dashed line), and the equivalent wind velocity $V^*$ (red line). (For interpretation of the references to colour in this figure legend, the reader is referred to the web version of this article.)

where we observe that if the meridional wind velocities are larger than $\sim 0.025$ m s$^{-1}$ then dynamics is the main factor controlling the haze distribution in the atmosphere. Thus, these results suggest that the short-term observed seasonal variations in the haze distribution are likely due to the transport of haze particles by dynamics and with wind velocities that should be greater than $\sim 0.025$ m s$^{-1}$. This velocity is a first approximation based on the timescale analyses.

## 4. Conclusions

We have used a microphysical model to simulate the haze formation and evolution in Uranus's atmosphere. These simulations were coupled with the NEMESIS radiative-transfer code to model infrared data from VLT/SINFONI and visible data from HST/Wide Field Camera 3, both acquired in 2014. The main goal of combining both models was to constrain the microphysical parameters to study the nature of Uranus's haze. Our simulations show that: 1) the eddy-diffusion coefficient $K$ has a little impact on the haze distribution in the atmosphere for the expected range of values of this parameter (the same conclusions were reported in Pollack et al., 1987); 2) the haze electric charge parameter $q$ is not well constrained with our observations, although our simulations show it must be smaller than 20 electrons per $\mu$m radius; 3) the haze production rate in the stratosphere is found to be between $\sim 3.10^{-16}$ and $3.10^{-15}$ kg m$^{-2}$ s$^{-1}$.

The $M_0$ range derived in this work is very similar to that found by Pollack et al. (1987) from Voyager-2 observations at similar latitudes. This result indicates that the elapsed time between the Voyager-2 observations in 1986 and the VLT/HST observations in 2014 is smaller than the timescales for haze particles to grow and fall. The analyses in section 3.3 have shown that these haze microphysics timescales are $>$ 30 years for pressure levels $>$ 0.1 bar. This indicates that any changes in the haze production rate resulting from variations in the solar illumination at the top of the atmosphere cannot affect the haze structure below the level of 0.1 bar of pressure on time scales $<$ 30 years. These results put key constraints on the observed seasonal changes in the haze structure after the 2007 equinox over the northern hemisphere (de Pater et al., 2015; Sromovsky et al., 2018). The observed short time scales for these changes suggest that we cannot explain them as being due to variations in the haze mass production due to increasing solar illumination at the north pole. Indeed, we have seen that the response of the haze to changes in its production rate is much too sluggish to explain these post equinox changes. Thus, dynamics may play a key role here by transporting haze particles from different regions of the planet. The magnitude of this meridional transport should be greater than the equivalent wind velocities given in Fig. 14 ($\sim 0.025$ ms$^{-1}$). This transport of haze particles requires also vertical wind velocities greater than annual average estimations given in Conrath et al. (1990) whose values are much smaller (by several orders of magnitude) than those given in Fig. 13. To further address this point, however, GCM models capable of simulating the transport of haze are required. These simulations, compared or coupled with haze microphysics, will determine how efficient dynamics is in distributing the haze in the atmosphere. These simulations may also explain the formation of the methane polar hole observed in 2014 (Toledo et al., 2018) since our timescale analyses suggest that its formation might be due to dynamics.

## Acknowledgements

The VLT/SINFONI observations were performed at the European Southern Observatory (ESO), Proposal 092.C-0187. The HST observations were made with the NASA/ESA Hubble Space Telescope under programs GO13937/14334. Support for this latter program was provided by NASA through a grant from the Space Telescope Science Institute, which is operated by the Association of Universities for Research in Astronomy, Inc., under NASA contract NAS5-26555. Daniel Toledo, Patrick Irwin and Nicholas Teanby acknowledge the support of

the UK Science and Technology Facilities Council. Glenn Orton acknowledges support from the National Aeronautics and Space Administration that were distributed to the Jet Propulsion Laboratory, California Institute of Technology. Telescope data are publicly available in ESO repository (http://archive.eso.org/eso/eso_archive_main.html).

## References

Atreya, S., Romani, P., 1985. Photochemistry and clouds of Jupiter, Saturn and Uranus. In: Recent Advances in Planetary Meteorology. 17. pp. 68.

Borysow, A., Frommhold, L., 1987. Collision-induced rototranslational absorption spectra of ch4-ch4 pairs at temperatures from 50 to 300 k. Astrophys. J. 318, 940–943.

Borysow, A., Frommhold, L., Moraldi, M., 1989. Collision-induced infrared spectra of h2-he pairs involving 0-1 vibrational transitions and temperatures from 18 to 7000 k. Astrophys. J. 336, 495–503.

Borysow, A., Borysow, J., Fu, Y., 2000. Semi-empirical model of collision-induced absorption spectra of h2–h2 complexes in the second overtone band of hydrogen at temperatures from 50 to 500 k. Icarus 145 (2), 601–608.

Cabane, M., Chassefiere, E., Israel, G., 1992. Formation and growth of photochemical aerosols in titan's atmosphere. Icarus 96 (2), 176–189.

Campargue, A., Wang, L., Mondelain, D., Kassi, S., Bézard, B., Lellouch, E., Coustenis, A., De Bergh, C., Hirtzig, M., Drossart, P., 2012. An empirical line list for methane in the 1.26–1.71μm region for planetary investigations (t = 80–300 k). Application to titan. Icarus 219 (1), 110–128.

Cheng, A.F., Summers, M.E., Gladstone, G.R., Strobel, D.F., Young, L.A., Lavvas, P., Kammer, J.A., Lisse, C.M., Parker, A.H., Young, E.F., et al., 2017. Haze in pluto's atmosphere. Icarus 290, 112–133.

Colina, L., Bohlin, R.C., Castelli, F., 1996. The 0.12–2.5 micron absolute flux distribution of the sun for comparison with solar analog stars. Astron. J. 112, 307.

Conrath, B.J., Gierasch, P.J., Leroy, S.S., 1990. Temperature and circulation in the stratosphere of the outer planets. Icarus 83 (2), 255–281.

Dressel, L., 2012. Wide Field Camera 3 Instrument Handbook for Cycle 21 V. 5.0. Wide Field Camera 3. HST Instrument Handbook.

Fouchet, T., Lellouch, E., Feuchtgruber, H., 2003. The hydrogen ortho-to-para ratio in the stratospheres of the giant planets. Icarus 161 (1), 127–143.

Fuchs, N., 1964. The Mechanics of Aerosols 1964. Pergamon, New York.

Irwin, P., Teanby, N., De Kok, R., Fletcher, L., Howett, C., Tsang, C., Wilson, C., Calcutt, S., Nixon, C., Parrish, P., 2008. The nemesis planetary atmosphere radiative transfer and retrieval tool. J. Quant. Spectrosc. Radiat. Transf. 109 (6), 1136–1150.

Irwin, P., de Bergh, C., Courtin, R., Bézard, B., Teanby, N., Davis, G., Fletcher, L., Orton, G., Calcutt, S., Tice, D., et al., 2012a. The application of new methane line absorption data to gemini-n/nifs and kpno/fts observations of uranus near-infrared spectrum. Icarus 220 (2), 369–382.

Irwin, P., Teanby, N., Davis, G., Fletcher, L., Orton, G., Calcutt, S., Tice, D., Hurley, J., 2012b. Further seasonal changes in uranus cloud structure observed by gemini-north and ukirt. Icarus 218 (1), 47–55.

Irwin, P.G., Wong, M.H., Simon, A.A., Orton, G., Toledo, D., 2017. Hst/wfc3 observations of uranus 2014 storm clouds and comparison with vlt/sinfoni and irtf/spex observations. Icarus 288, 99–119.

Irwin, P.G., Toledo, D., Garland, R., Teanby, N.A., Fletcher, L.N., Orton, G.A., Bézard, B., 2018. Detection of hydrogen sulfide above the clouds in uranus's atmosphere. Nature Astronomy 2 (5), 420.

Irwin, P.G.J., Fletcher, L.N., Read, P.L., Tice, D., de Pater, I., Orton, G.S., Teanby, N.A., Davis, G.R., 2016. Spectral analysis of uranus 2014 bright storm with vlt/sinfoni. Icarus 264, 72–89.

Karkoschka, E., Tomasko, M., 2009. The haze and methane distributions on uranus from HST-STIS spectroscopy. Icarus 202 (1), 287–309.

Karkoschka, E., Tomasko, M.G., 2010. Methane absorption coefficients for the jovian planets from laboratory, Huygens, and HST data. Icarus 205 (2), 674–694.

Moses, J., Fouchet, T., Bézard, B., Gladstone, G., Lellouch, E., Feuchtgruber, H., 2005. Photochemistry and diffusion in Jupiter's stratosphere: constraints from ISO observations and comparisons with other giant planets. Journal of Geophysical Research: Planets 110 (E8).

Moses, J.I., Fletcher, L.N., Greathouse, T.K., Orton, G.S., Hue, V., 2018. Seasonal stratospheric photochemistry on uranus and neptune. Icarus 307, 124–145.

Orton, G.S., Fletcher, L.N., Moses, J.I., Mainzer, A.K., Hines, D., Hammel, H.B., Martin-Torres, F.J., Burgdorf, M., Merlet, C., Line, M.R., 2014a. Mid-infrared spectroscopy of uranus from the Spitzer infrared spectrometer: 1. Determination of the mean temperature structure of the upper troposphere and stratosphere. Icarus 243, 494–513.

Orton, G.S., Moses, J.I., Fletcher, L.N., Mainzer, A.K., Hines, D., Hammel, H.B., Martin-Torres, J., Burgdorf, M., Merlet, C., Line, M.R., 2014b. Mid-infrared spectroscopy of uranus from the Spitzer infrared spectrometer: 2. Determination of the mean composition of the upper troposphere and stratosphere. Icarus 243, 471–493.

de Pater, I., Sromovsky, L., Fry, P., Hammel, H.B., Baranec, C., Sayanagi, K.M., 2015. Record-breaking storm activity on uranus in 2014. Icarus 252, 121–128.

Pollack, J.B., Rages, K., Pope, S.K., Tomasko, M.G., Romani, P.N., Atreya, S.K., 1987. Nature of the stratospheric haze on uranus: evidence for condensed hydrocarbons. J. Geophys. Res. Space Physics 92 (A13), 15037–15065.

Rages, K., Pollack, J.B., Tomasko, M.G., Doose, L.R., 1991. Properties of scatterers in the troposphere and lower stratosphere of uranus based on voyager imaging data. Icarus 89 (2), 359–376.

Rannou, P., Hourdin, F., McKay, C., Luz, D., 2004. A coupled dynamics-microphysics model of titan's atmosphere. Icarus 170 (2), 443–462.

Ryan Jr., R., Deustua, S., Sosey, M., Anderson, J., Baggett, S., Bajaj, V., Bourque, M., Bowers, A., Dahlen, T., Durbin, M., et al., 2016. The updated calibration pipeline for WFC3/UVIS: a reference guide to Calwf3 (version 3.3). In: Instrument Science Report WFC3-2016-001.

Sheik-Bahae, M., 2005. Nonlinear optics basics. Kramers-Kronig relations in nonlinear optics. In: Encyclopedia of Modern Optics, pp. 234–239.

Sromovsky, L., Fry, P., Kim, J.H., 2011. Methane on uranus: the case for a compact ch4 cloud layer at low latitudes and a severe ch4 depletion at high-latitudes based on reanalysis of voyager occultation measurements and STIS spectroscopy. Icarus 215 (1), 292–312.

Sromovsky, L.A., Karkoschka, E., Fry, P.M., de Pater, I., Hammel, H.B., 2018. The Methane Distribution and Polar Brightening on Uranus Based on HST/STIS, Keck/NIRC2, and IRTF/SpeX Observations through 2015. arXiv preprint. arXiv:1806.01154.

Toledo, D., Irwin, P.G., Teanby, N.A., Simon, A.A., Wong, M.H., Orton, G.S., 2018. Uranus's northern polar cap in 2014. Geophys. Res. Lett. 45 (11), 5329–5335.

Toon, O., Turco, R., Westphal, D., Malone, R., Liu, M., 1988. A multidimensional model for aerosols: description of computational analogs. J. Atmos. Sci. 45 (15), 2123–2144.

Toon, O., McKay, C., Griffith, C., Turco, R., 1992. A physical model of titan's aerosols. Icarus 95 (1), 24–53.

Toon, O.B., Turco, R., Pollack, J.B., 1980. A physical model of titan's clouds. Icarus 43 (3), 260–282.

Tyler, G., Sweetnam, D., Anderson, J., Campbell, J., Eshleman, V., Hinson, D., Levy, G., Lindal, G., Marouf, E., Simpson, R., 1986. Voyager 2 radio science observations of the uranian system: atmosphere, rings, and satellites. Science 233 (4759), 79–84.

Wong, M., Simon, A., Orton, G., de Pater, I., Sayanagi, K., 2015. Hubble's long-term opal (outer planet atmospheres legacy) program observes cloud activity on uranus. In: Lunar and Planetary Science Conference. vol. 46. p. 2606.

Wong, M.H., 2010. Fringing in the WFC3/UVIS detector. In: Hubble after SM4. Preparing JWST.

Zheng, C., Borysow, A., 1995. Modeling of collision-induced infrared absorption spectra of h2 pairs in the first overtone band at temperatures from 20 to 500 k. Icarus 113 (1), 84–90.